ACCEPTED ARTICLE PREVIEW

Accepted Article Preview: Published ahead of online publication

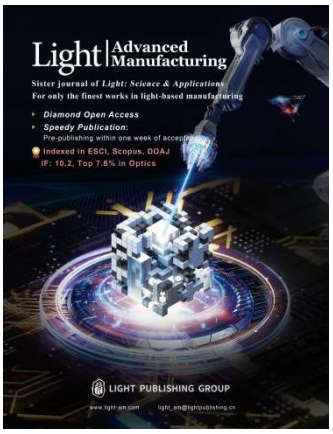

Sector-Rotational Structured Illumination Microscope for Large Field-of-View Super-Resolution Imaging

Han Wang, Ruijie Cao, Wenyi Wang, Shu Gao, Jianming Rong, Lijun Li, Maoqi Tian, Yunzhe Fu, Wei Ren, Donghyun Kim, Xuantao Su, Meiqi Li, and Peng Xi

Cite this article as: Han Wang, Ruijie Cao, Wenyi Wang, Shu Gao, Jianming Rong, Lijun Li, Maoqi Tian, Yunzhe Fu, Wei Ren, Donghyun Kim, Xuantao Su, Meiqi Li, Peng Xi. Sector-Rotational Structured Illumination Microscope for Large Field-of-View Super-Resolution Imaging. *Light: Advanced Manufacturing* accepted article preview 03 July, 2026; doi: 10.37188/lam.2026.121

This is a PDF file of an unedited peer-reviewed manuscript that has been accepted for publication. LAM are providing this early version of the manuscript as a service to our customers. The manuscript will undergo copyediting, typesetting and a proof review before it is published in its final form. Please note that during the production process errors may be discovered which could affect the content, and all legal disclaimers apply.

Received 17 June 2026; revised 02 July 2026; accepted 03 July 2026;
Accepted article preview online 03 July 2026

Accepted Manuscript

ACCEPTED ARTICLE PREVIEW

Sector-Rotational Structured Illumination Microscope for Large Field-of-View Super-Resolution Imaging

Han Wang[1,†], Ruijie Cao[1,†,*], Wenyi Wang[2], Shu Gao[1], Jianming Rong[1], Lijun Li[3], Maoqi Tian[4], Yunzhe Fu[1], Wei Ren[1], Donghyun Kim[5], Xuantao Su[6], Meiqi Li[7,*], and Peng Xi[1,2,*]

[1] College of Future Technology, National Biomedical Imaging Center, Peking University, Beijing, 100871, China;
[2] Airy Technologies Co. Ltd., Beijing, 100081, China;
[3] College of Chemistry and Materials Science, Hebei University, Baoding, 071002, China;
[4] School of Basic Medical Sciences, Capital Medical University, Beijing, 100069, China;
[5] School of Electrical and Electronic Engineering, Yonsei University, 50 Yonsei-Ro, Seodaemun-Gu, Seoul, 03722, Korea;
[6] School of Integrated Circuits, Shandong University, Jinan, 250101, China;
[7] School of Life Sciences, Peking University, Beijing, 100871, China.
[†] These co-authors contribute to this work equally.
* Email address: caoruijie.edu@gmail.com; limeiqi@pku.edu.cn; xipeng@pku.edu.cn.

Abstract

Structured illumination microscopy (SIM) doubles the lateral resolution compared with wide-field fluorescence microscopy. However, the fast modulation of structured illumination patterns is typically highly dependent on pixelated digital devices, which suffer from low optical efficiency, self-diffraction noise, and high costs. Here, we present a SEctor-ROtational SIM (Sero-SIM), which integrates the modulation of the illumination direction and phase shift into a single sector-rotational transmissive grating, achieving an approximately twofold resolution enhancement at a very low cost and minimal control complexity. Moreover, by incorporating a pyramidal lens into the optical setup, we decouple the sector size from the field of view (FOV), expanding the FOV by more than 13 times. We evaluated the performance of Sero-SIM using high-fidelity imaging of diverse subcellular structures in both fixed samples and live cells. The capability of large-FOV super-resolution imaging endows Sero-SIM with a strong potential for applications spanning multiple spatial scales, from pathological tissues and cell populations to single cells and subcellular organelles. Altogether, Sero-SIM introduces a distinctive and practical approach for SIM implementation.

Keywords

Grating roulette, Structured illumination microscopy, Cost efficient, Super-resolution imaging

Structured illumination microscopy (SIM) plays an essential role in subcellular super-resolution imaging and long-term live-cell imaging owing to its low phototoxicity, high compatibility with conventional fluorophores, and high spatiotemporal resolution.[1-5] In classical SIM, sinusoidal illumination fringes with a predefined spatial frequency and phase are superimposed onto the specimen, generating low-frequency moiré fringes that encode high-frequency information. By introducing three phase-shift steps, the fine structural details beyond the diffraction limit can be computationally reconstructed. The illumination fringes are typically rotated two or three times at equal angular intervals to achieve isotropic resolution.

Various methods have been developed to modulate the orientation and phase of structured illumination patterns. In early SIM implementations, diffraction gratings, rotation mounts, and piezoelectric translation stages were used to precisely control the direction and optical path difference of diffracted beams, thereby generating high-frequency interference fringes at the sample plane.[6-10] Recently, spatial light modulators (SLMs) have become mainstream core devices in SIM owing to their precise and programmable light control.[11-22] However, SLM-based systems, often

Accepted Manuscript

ACCEPTED ARTICLE PREVIEW

combined with liquid-crystal variable retarders and polarisation beam splitters, are typically expensive and require complex synchronisation and control, which limit their accessibility and broad adoption. In comparison, digital micromirror devices (DMDs) offer higher refresh rates and lower costs. In SIM, DMDs can serve as either projectors or blazed gratings, generating sinusoidal patterns through projection or interference.[5,23-29] Nevertheless, the discrete pixel structures of these digital devices result in low light efficiencies, self-diffraction orders, and beam distortions (Fig. S1, Supp. Note 1). Therefore, the promotion and widespread application of SIM remain are constrained by high technical and financial barriers. Thus, a low-cost yet high-performance SIM system is required to improve the accessibility of super-resolution imaging.

In this study, we integrated the modulation of the illumination direction and phase shift into a single sector-rotational grating roulette, developing the SEctor-ROtational SIM (Sero-SIM) system. Sero-SIM enables super-resolution fluorescence imaging at a very low expense, with minimal control complexity and excellent scalability. The roulette can be rotated to different sectors to achieve both phase shifting and angle switching. Benefitting from the high diffraction efficiency and non-pixelated pattern of the transmissive grating, the required laser power can be reduced to 25% of that in SLM-based systems or 62.5% that in DMD-based systems. Using an oil-immersion objective with a numerical aperture (NA) of 1.45, we achieved lateral resolutions of 128.07 nm (473 nm excitation) and 143.68 nm (561 nm excitation), corresponding to an enhancement of about twofold beyond the diffraction limit. To further improve the imaging throughput, we decoupled the field of view (FOV) from the illumination spot size by introducing a specifically designed pyramidal lens,[30] enabling a large FOV of 107 μm × 107 μm (1650 pixels × 1650 pixels) under a 100× objective. By switching the objectives of different magnifications and NAs, Sero-SIM provides super-resolution imaging across multiple spatial scales with an ultra-large FOV, extending SIM to mesoscopic applications such as tissue-section examination and cell-population observation. Moreover, time-lapse live-cell imaging of microtubules and actin filaments demonstrated the low phototoxicity, robustness, and high resolution of Sero-SIM, confirming its potential for visualising dynamic physiological processes within subcellular organelles.

Results

Development of Sero-SIM

Two-beam interference is a classical approach for generating structured illumination patterns on a specimen. Typically, a laser beam is incident on a diffraction element, and the ±1st-order diffracted beams remain highly coherent. Therefore, the core challenge in SIM implementation is to periodically control both the diffraction direction and optical path difference between the two beams.

In SIM implementations, mechanical modulation, such as rotating or translating diffraction gratings, is limited by the precision and speed constraints of complex mechanical actuation. In contrast, digital modulators such as SLMs and DMDs enable high-speed optical control but introduce other challenges: Their discrete pixelated structures inherently generate undesired peaks in the frequency domain, leading to reconstruction artefacts, reduced diffraction efficiency, and wavefront distortion (Fig. S1, Supp. Note 1). These challenges necessitate careful calibration and complex compensation.[31-33] Moreover, the typical diffraction efficiency of digital devices is below 10%, requiring a substantially higher laser power to compensate for the energy losses. These limitations, combined with their high cost and complex control logic, restrict their practicality in many applications.

To address these problems, we mapped the nine structured illumination patterns required for SIM reconstruction onto binary grating sectors to form a grating roulette. By rotating the roulette at equal angular intervals, we can switch both the diffraction direction and optical path difference of the interfering beams. The grating roulette serves as the core light-modulation element of the Sero-SIM system (Fig. 1a), offering high diffraction efficiency, uniform mechanical motion control, and extremely low cost. Furthermore, to achieve a larger FOV, we introduced a pyramidal lens into the system design, which refracts the ±1st-order beams without altering their collimation, effectively increasing the *effective diffraction angle* and enabling large-FOV super-resolution imaging (Fig. 1a, Fig. S2c, Supp. Note 2). Thus, the cost of the key components in Sero-SIM is reduced by an order of magnitude compared with other SIM systems (Supp. Table 1).

In Sero-SIM, the incident beam is directed onto the centre of a specific sector, referred to as the working sector, which is immediately below the centre of the grating roulette (Fig. 1a, b). During rotation, the incident beam remains stationary, and each of the nine sectors sequentially serves as the working sector. The nine sectors are divided into three groups, with each group sharing the same pattern orientation but exhibiting equally spaced phase shifts (Fig. 1b, i–ii). After diffraction, the beam is split along the pattern direction (Fig. 1b, iii–v), and the phase configuration of each

grating sector modulates the optical-path difference between the ±1st-order beams, thereby generating the corresponding phase shift of the interference fringes on the sample plane. The grating roulette is driven by a

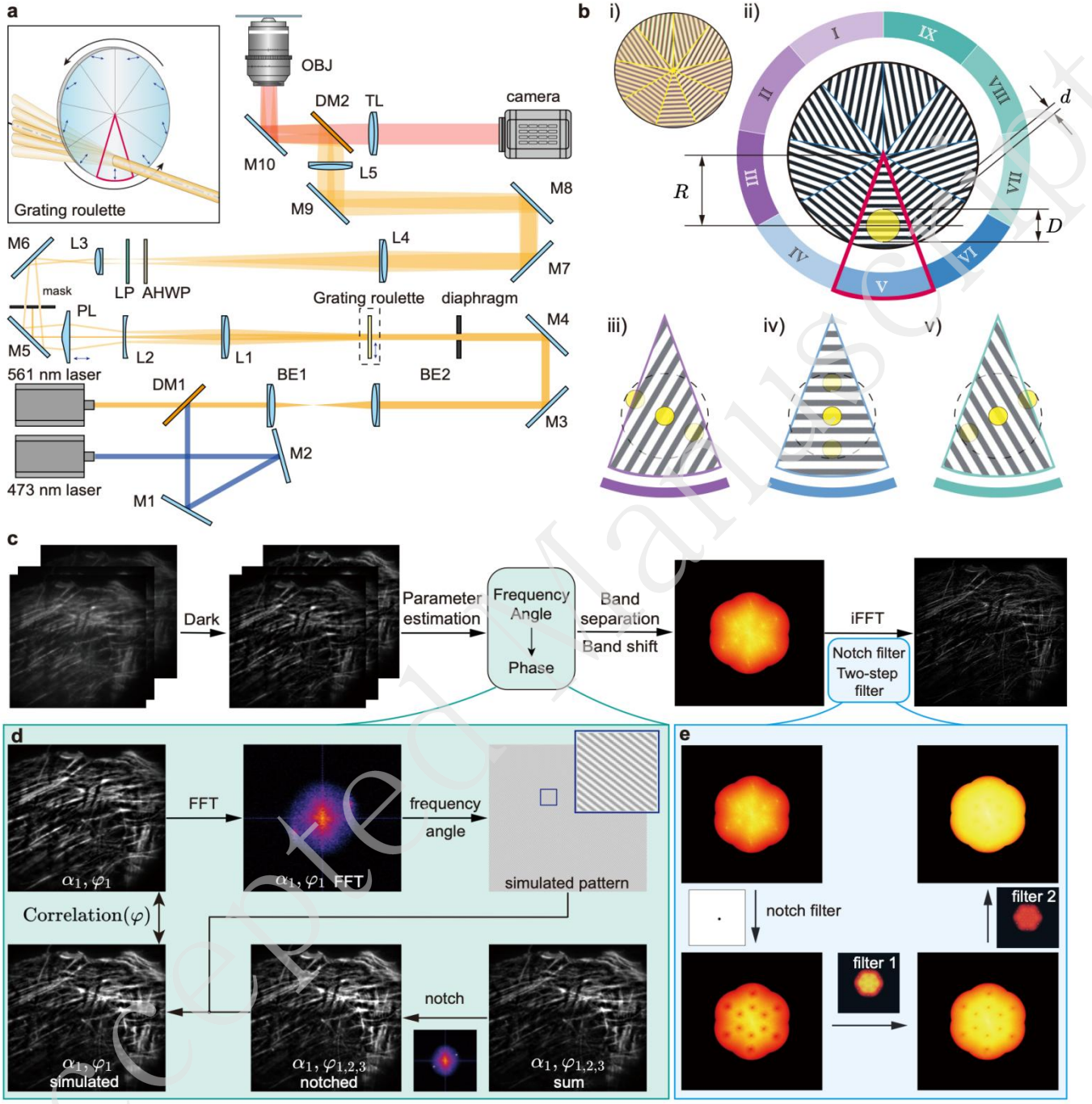

Fig. 1 | Sero-SIM principle and reconstruction algorithms. a, Schematic of Sero-SIM. The illumination beams of 561 nm are shown in orange, those of 473 nm in blue, and the fluorescence emission red. The 473 nm beams share a similar optical path to the 561 nm excitation beam, except for a slight chromatic aberration caused by diffraction and refraction. The variation in the diffraction direction and phase relationship of the diffracted beams is achieved by rotating different grating sectors into the working position, as shown in red. In the box, the blue arrows marked in the different sector regions indicate the diffraction directions of the grating. M1-M10, mirrors; L1-L3, lenses; BE1 and BE2, beam expander; DM1 and DM2, long-pass dichroic mirrors; PL, pyramidal lens; LP, linear polariser; AHWP, achromatic six-segmented half-wave plate; TL, tube lens; OBJ, objective. **b**, Details of the grating roulette. i) Photograph of the grating roulette under a 20× bright-field microscope. ii) Design of the grating roulette. The illumination beam is shown as the yellow circle with a diameter of D. The centre of the roulette is higher than the illumination beam by a distance of R. The grating with a grating constant d is equally divided into nine sectors, noted as sectors I to IX. The red sector marks the working sector. The nine sectors are categorized into three groups according to their stripe orientations, as shown in purple (I–III), blue (IV–VI), and green (VII–IX), respectively. When in the working position, gratings from different groups diffract the incident beam into distinct directions, as illustrated in iii, iv, and v. Within the same group, the gratings exhibit different phases when in working position, thereby affecting the light path difference between the ±1st-order diffracted beams. In iii), iv), and v), the three yellow circles indicate the -1st, 0th, and +1st diffracted beams. The diffraction directions are in line with the directions of the grating patterns. **c**, Full reconstruction algorithm flow of Sero-SIM. **d**, Flow of the spatial lock-in phase retrieval algorithm. **e**, Two-step filter containing dual notch filters applied to optimize the frequency components, and inverse Fourier transform is performed to

piezoelectric rotation mount, which performs nine uniform 40° rotations during a full image-acquisition cycle; thus, one complete revolution yields a full set of nine raw images. The rotary mount is the only active component in the system, besides the camera, and its synchronisation with the camera is achieved using a simple MATLAB programme, substantially reducing the system's control complexity (Fig. S3 and Supp. Note 3).

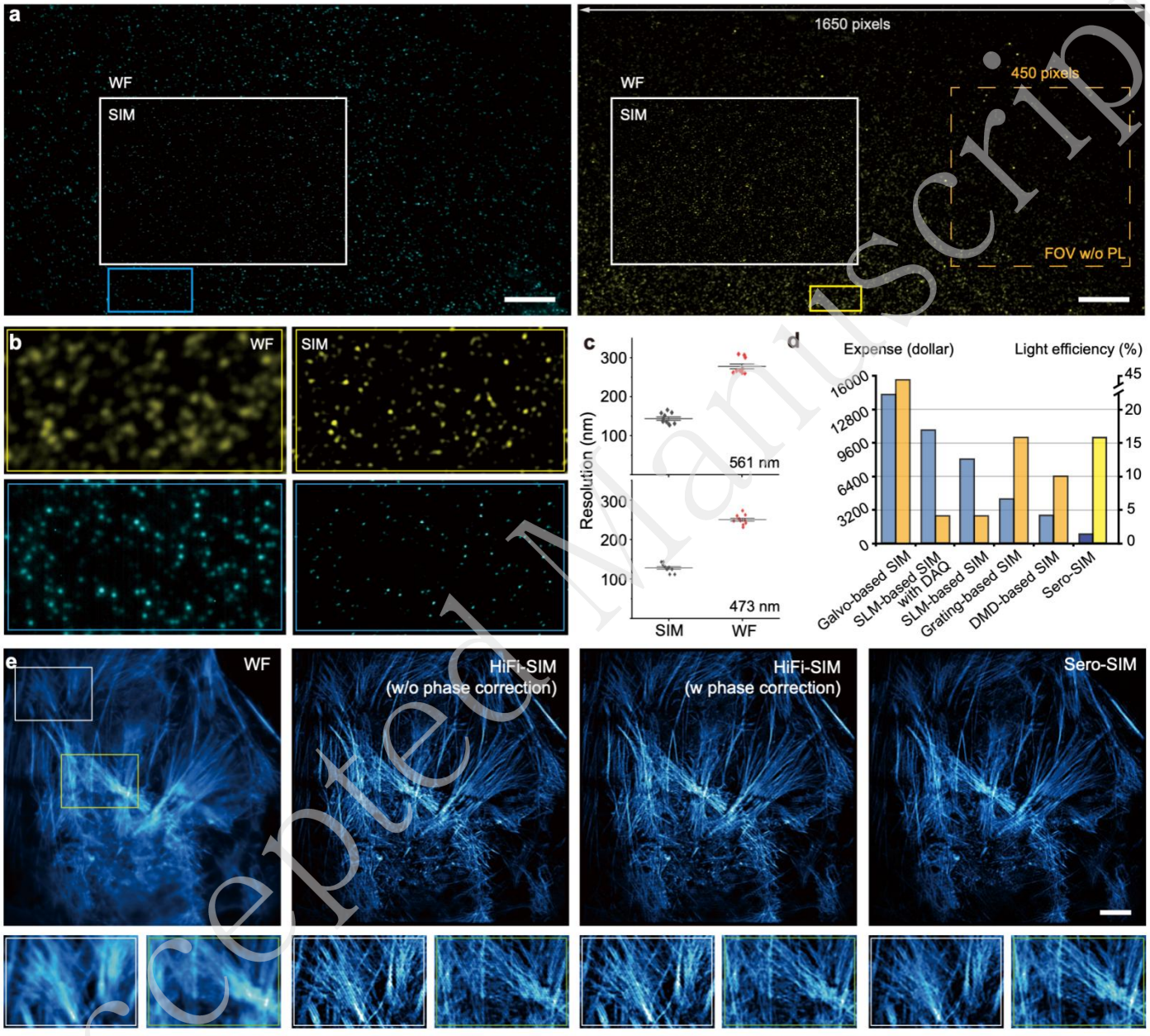

Fig. 2 | System characterization and algorithm performance. a, 40-nm fluorescent beads with 473 nm (left) and 561 nm (right) excitation. Imaging FOV achieves 1650 pixels × 1650 pixels. An FOV of systems without a pyramidal lens is shown in the golden dashed box for comparison. **b**, Comparison of details between wide-field fluorescent images (left) and Sero-SIM results (right). **c**, Resolution improvement of Sero-SIM under 473 nm and 561 nm excitation. **d**, Key component expense (left blue columns) and diffraction efficiency (right cyan columns) comparison among various SIM techniques. The yellow and green columns of Sero-SIM present the lowest expense and high diffraction efficiency. **e**, Algorithm performance evaluation. Comparison between wide-field images, traditional 2D-SIM reconstruction without phase correction, traditional 2D-SIM with phase correction, and Sero-SIM results. The bottom shows the magnified zones of the white and yellow boxes. Scale bars: 10 μm (**a**); 4 μm (**e**).

Accepted Manuscript

ACCEPTED ARTICLE PREVIEW

Reconstruction algorithm of Sero-SIM

In SIM reconstruction, evenly spaced phases of 0, 2π/3, 4π/3 are generally preferred such that the summation of raw images is equivalent to the widefield fluorescent image. Conventional super-resolution reconstruction algorithms typically assume the phase shift by default as 2π/3.[10] However, the rotation mount in Sero-SIM exhibits finite positioning accuracy and repeatability, leading to small phase-shift uncertainty of the structured patterns on the sample plane. Under an appropriate design of the grating roulette, the phase uncertainty is *under control* and *acceptable*, and relatively stable phases can be obtained during the working process (Supp. Note 4). However, that does not mean that we have *ideal* phases; the phase-shift value between adjacent patterns does not precisely equal 2π/3 (Fig. S4). Most open-source algorithms do not consider such uneven phase shifts, which leads to severe artefacts after reconstruction (Fig. S5, Supp. Note 5). In contrast, our reconstruction algorithm considers the phase uncertainty by estimating the precise phase value of each raw frame in advance and in a few specific steps (Fig. 1c). Simulations indicate that our reconstruction algorithm is tolerant to such deviations (Fig. S6, S7, Supp. Note 5) with good linearity (Fig. S8, Supp. Note 5). Raw images with *moderate* phase-shift uncertainty yield reconstruction results nearly identical to the ideal case (Fig. S4), except under extreme conditions where the three phases are too close to each other (Fig. S4).[30]

In parallel, the *even phase default* is widely applied in traditional SIM reconstruction algorithms, such as fairSIM[34,35], HiFi-SIM[36], dSIM[37], PCA-SIM[38], and Lock-in-SIM[39]. Therefore, most algorithms no longer accommodate Sero-SIM data owing to the phase uncertainty in the roulette-based system. In our reconstruction algorithm (Fig. 1c), dark sectioning is applied for background removal.[40] Thereafter, the illumination frequency, angle, and phase parameters are calculated. The frequency bands are separated and shifted in the frequency domain. Subsequently, a designed notch filter and a two-step filter are applied to suppress the artefacts.

Specifically, the main differences from traditional algorithms are phase estimation and filters. For phase estimation, we propose a *spatial lock-in phase retrieval algorithm* that estimates the phase of a structured illumination pattern after evaluating the frequency and angle of each illumination pattern. First, we generate a simulated wide-field image by summing three raw images acquired at the same illumination angle (Fig. 1d, Supp. Note 5). After notch filtering, which is necessary because of uneven phase spacing, the simulated wide-field image is modulated with simulated illumination patterns. We then compute the correlation between the modulated image and the corresponding raw frame to identify the accurate phase corresponding to the correlation maximum (Fig. S9, Supp. Note 5). This frame-by-frame phase estimation ensures correct phase-matrix separation, although the evaluated phases may differ slightly from their true values. As shown in Fig. S6, we have demonstrated that our spatial lock-in phase retrieval method surpasses the existing methods, particularly under conditions such as a low signal-to-noise ratio, low modulation depth, or high modulation frequency; our method also ensures reconstruction fidelity. To mitigate the frequency artefacts caused by deviations of the evaluated phases from the true values, we apply a dual-notch filter to suppress the residual frequency peaks (Fig. 1e). In addition, we introduce a two-step filtering strategy for artefact reduction while preserving weak signals, combined with a dark sectioning pre-processing procedure to remove defocused background noise. The optimisation pipeline guarantees high-fidelity super-resolution Sero-SIM reconstructions with suppressed artefacts.[40]

Characterization of Sero-SIM

The resolution of Sero-SIM was characterised using 40-nm fluorescent beads by measuring the full width at half maximum (FWHM) of a reconstructed point spread function (PSF) (Fig. 2a). Local detail comparisons further demonstrated the remarkable resolution improvement achieved by Sero-SIM: neighbouring beads indistinguishable in wide-field images are clearly resolved as separate points after reconstruction (Fig. 2b). Under wide-field illumination, the resolutions were 250.34 nm (473 nm excitation) and 277.66 nm (561 nm excitation). After SIM reconstruction, they improved to 128.07 nm and 143.69 nm, corresponding to approximately twofold enhancements (Fig. 2c) while maintaining a substantially larger imaging field compared with conventional SIM.

Another key advantage of Sero-SIM is its cost-effectiveness and high diffraction efficiency (Fig. 2d). Without relying on pixelated digital modulation devices, such as SLMs, DMDs, or galvo mirrors, the cost of Sero-SIM core components is extremely low, at less than USD 1000 (Supp. Table 1). Moreover, the continuous binary stripes on the grating roulette provide a 60% higher diffraction frequency than DMD-based approaches and a 400% increase relative

ACCEPTED ARTICLE PREVIEW

to amplitude-modulation SLMs. For systems with higher light efficiency (e.g. galvo-based SIM), the element costs are tens of times higher than those of a grating roulette, which poses a barrier to the accessibility and affordability of SIM.

As shown in Fig. 2e, conventional SIM reconstruction algorithms such as HiFi-SIM assume evenly spaced phase shifts and fail to reconstruct Sero-SIM images because of the inherent phase uncertainty. By applying the proposed frame-by-frame phase estimation, line-shaped artefacts are largely eliminated owing to the accurate phase separation. In addition, a dual-notch filter and an improved two-step filtering procedure were implemented for reconstruction optimisation, further reducing the artefacts. Consequently, actin filaments can be reconstructed with high fidelity and minimal artefacts (Fig. 2e).

Visualizing subcellular details with Sero-SIM

The super-resolution and low phototoxicity of SIM make it an indispensable tool for subcellular imaging. To further verify the biological imaging performance of Sero-SIM, we labelled nucleoporin (Nup) in COS-7 cells and visualized the nuclear pore complexes (NPCs), achieving a resolution of approximately 158.4 nm, representing a 1.72× improvement over the 272.5 nm resolution of wide-field fluorescence imaging (Fig. 3a, b). These results demonstrate the strong potential of Sero-SIM in advanced biological research.

We labelled tubulin in U2OS cells and imaged the microtubules under 561 nm excitation (Fig. 3c). Compared with wide-field fluorescence images, Sero-SIM clearly resolved the dense, intersecting microtubule network across the entire cell, achieving a resolution of 145.1 nm, corresponding to a 1.85-fold resolution enhancement (Fig. S10). In regions where the microtubules were tightly bundled, wide-field microscopy failed to distinguish between adjacent or crossing filaments, whereas Sero-SIM unambiguously delineated individual filament boundaries and orientations over a substantially larger FOV (Fig. 3d). This fine structural separation enables the quantitative analysis of cytoskeletal organisation and filament distribution, which are crucial for understanding intracellular transport and mechanical stability.

Theoretically, most fluorescent emitters behave as electric dipoles, and their orientations are closely correlated with the direction of their biological structures.[41-43] Equipped with stationary linear polarisers and pizza-waveplates, Sero-SIM is compatible with the polarised SIM (pSIM) modality, enabling further analysis of the fluorophore orientation by mapping emitters in the spatio-angular hyperspace. pSIM simultaneously retrieved the spatial ultrastructure and fluorophore dipole orientation.[44,45] We labelled actin filaments in U2OS cells with Lifeact-EGFP, and the pSIM results revealed that the polarisation orientations of the fluorophores were parallel to the directions of the actin filaments (Fig. 3e).

Furthermore, we evaluated the dual-colour super-resolution capability of Sero-SIM by imaging immunolabelled synaptonemal complexes (SCs) in mouse spermatocyte nuclei at the pachytene phase of meiotic prophase. An SC is a tripartite protein structure comprising two lateral elements, a central element, and numerous transverse filaments that

Accepted Manuscript

ACCEPTED ARTICLE PREVIEW

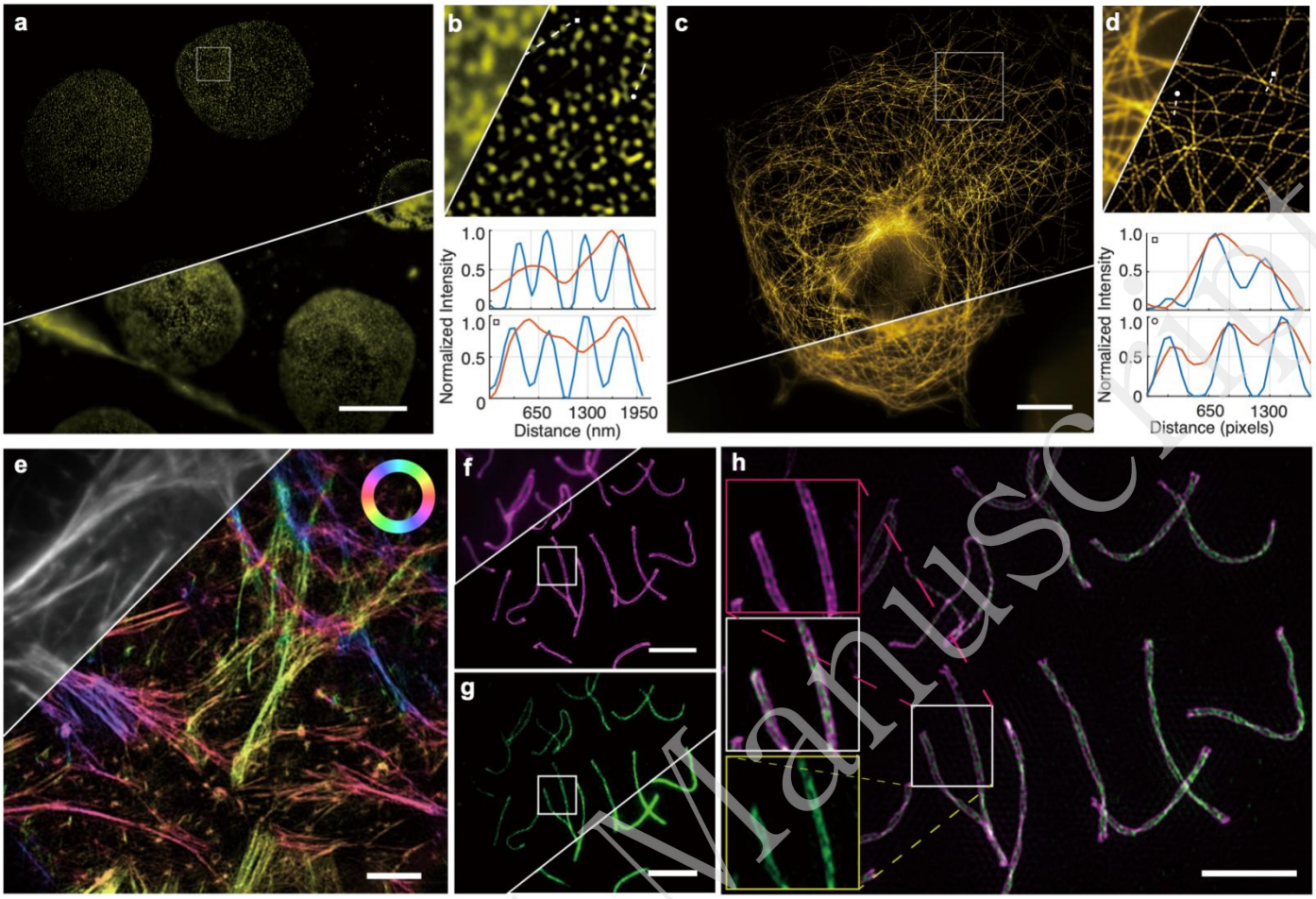

Fig. 3 | Subcellular structure visualization enabled by Sero-SIM. a, Nuclear pore complexes in COS-7 cells. Sero-SIM possesses an FOV of approximately 70 μm × 70 μm, enabling simultaneous imaging of a group of cells. **b**, Local details of NPC imaging results in the white box in (a). Intensity distribution comparison between wide-field and super-resolution results shows substantial resolution improvement. **c**, Microtubules in U2OS cells. Sero-SIM presents a complete network all over the cell. **d**, Local details of the microtubule network in the white box in (c). Intensity distribution comparison shows significant resolution enhancement. **e**, pSIM imaging of actin filaments in U2OS cells enabled by Sero-SIM. **f**, Immunolabelled synaptonemal complexes (SCs) in mouse spermatocyte nuclei in the pachytene phase of meiotic prophase. Double-line structures are distinguished with Sero-SIM under 561 nm excitation. **g**, Immunolabelled SCs under 473 nm excitation. Fine structures are clearly shown in super-resolution images, compared with a single line in wide-field images. **h**, Super-resolution imaging of SC with dual-colour Sero-SIM. (h) Superposition of (f) and (g). Details in the white boxes in (f, g, and h) are shown in the three boxes on the left. Scale bars: 10 μm (**a, c, f, g, h**); 4 μm (**e**).

interconnect the two sides. SYCP3 proteins, excitable by a 561 nm laser, are located within the lateral element approximately 220 nm apart, whereas SYCP1 dimers reside between SYCP3 proteins and can be excited with a 473 nm laser.[46] Under 561 nm excitation, Sero-SIM distinctly resolved the twisted double-line morphology of the SCs, whereas wide-field images showed only a single blurred line (Fig. 3f). Excitation at 473 nm revealed inner structural details corresponding to the central element and transverse filaments located between the two lateral lines (Fig. 3g). The dual-colour overlay clearly exhibited the characteristic organisation of an SC (Fig. 3h), validating the nanoscale-resolving capability of Sero-SIM. By integrating laser sources with multiple wavelengths and slightly adjusting the position of the pyramidal lens, the system can be readily extended to multi-colour super-resolution imaging (Fig. S2d), thereby providing rich structural information on diverse subcellular organelles and architectures.

Large-FOV multiscale super-resolution observation

By switching objectives with different magnifications and NAs, Sero-SIM enables super-resolution imaging across multiple spatial scales without any modification to the system architecture, thereby supporting biological and medical investigations at the organelle, cellular, and tissue levels.

Using 40×/0.95 NA and 100×/1.45 NA objectives, we imaged actin filaments in the same area of a fixed U2OS cell sample (Fig. 4a–f). As shown in Fig. 4b–e, Sero-SIM provided clear improvements in both image contrast and spatial

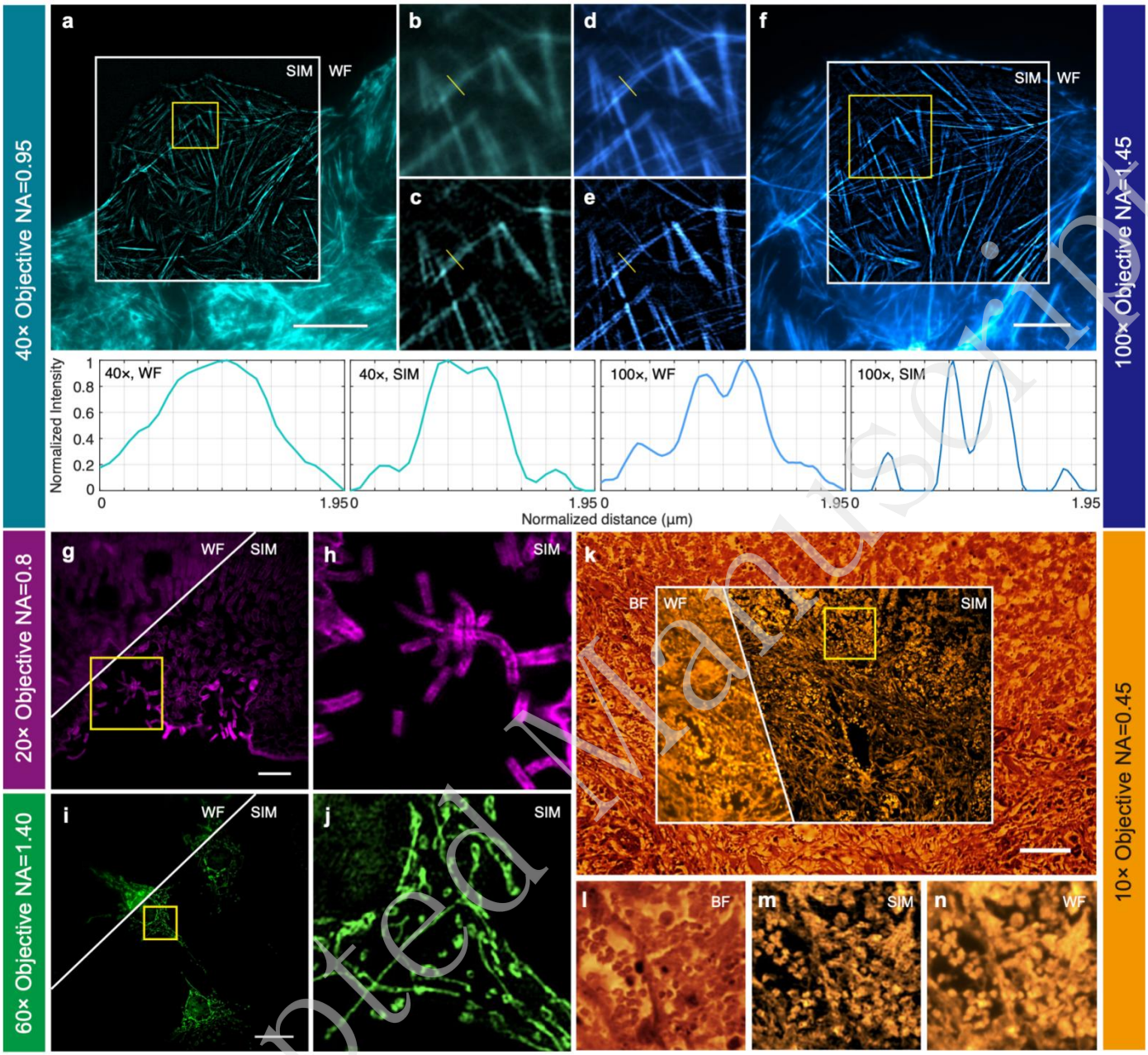

Fig. 4 | Multiscale super-resolution observation with Sero-SIM. a, Actin filaments in fixed U2OS cells under an objective of 40×, 0.95 NA. **b**, Local details of the wide-field image of the yellow box in (a). **c**, Local details of the super-resolution image of the yellow box in (a). **d**, Local details of the wide-field image of the yellow box in (f). e, Local details of the super-resolution image of the yellow box in (f). **f**, Actin filaments in the same area as (a) under an objective of 100×, 1.45 NA. **g, h**, Leaf of *Nerium oleander* (transverse section) under an objective of 20×, 0.80 NA and the local details in the yellow box. **i, j**, Mitochondria in fixed BPAE cells under an objective of 60×, 1.40 NA and the local details in the yellow box. **k**, Breast cancer tissue section under an objective of 10×, 0.40 NA. **l, m, n**, Bright field, super-resolution, and wide-field fluorescent images of the local details in the yellow box in (k), respectively. Scale bars: 25 μm (**a, i**); 10 μm (**f**); 50 μm (**g**); 100 μm (**k**).

resolution at both magnifications. When comparing Fig. 4b–d, the weak signals of the ultra-thin filaments were submerged in background noise in the low-NA raw images, limiting the recovery of super-resolved information. Nevertheless, Sero-SIM substantially suppressed the background and improved the visibility of the filamentous structures. However, for regions with stronger fluorescence signals, Sero-SIM reconstruction acquired with a 40× objective yields comparable resolution to the wide-field image captured with a 100× objective. For low-magnification objectives, the resolution enhancement is limited primarily by the effective pixel size projected onto the sample plane rather than by the period of the structured illumination patterns, whereas for high-magnification objectives, the structured illumination frequency is the most important limiting factor. Consequently, objectives with lower

Accepted Manuscript

ACCEPTED ARTICLE PREVIEW

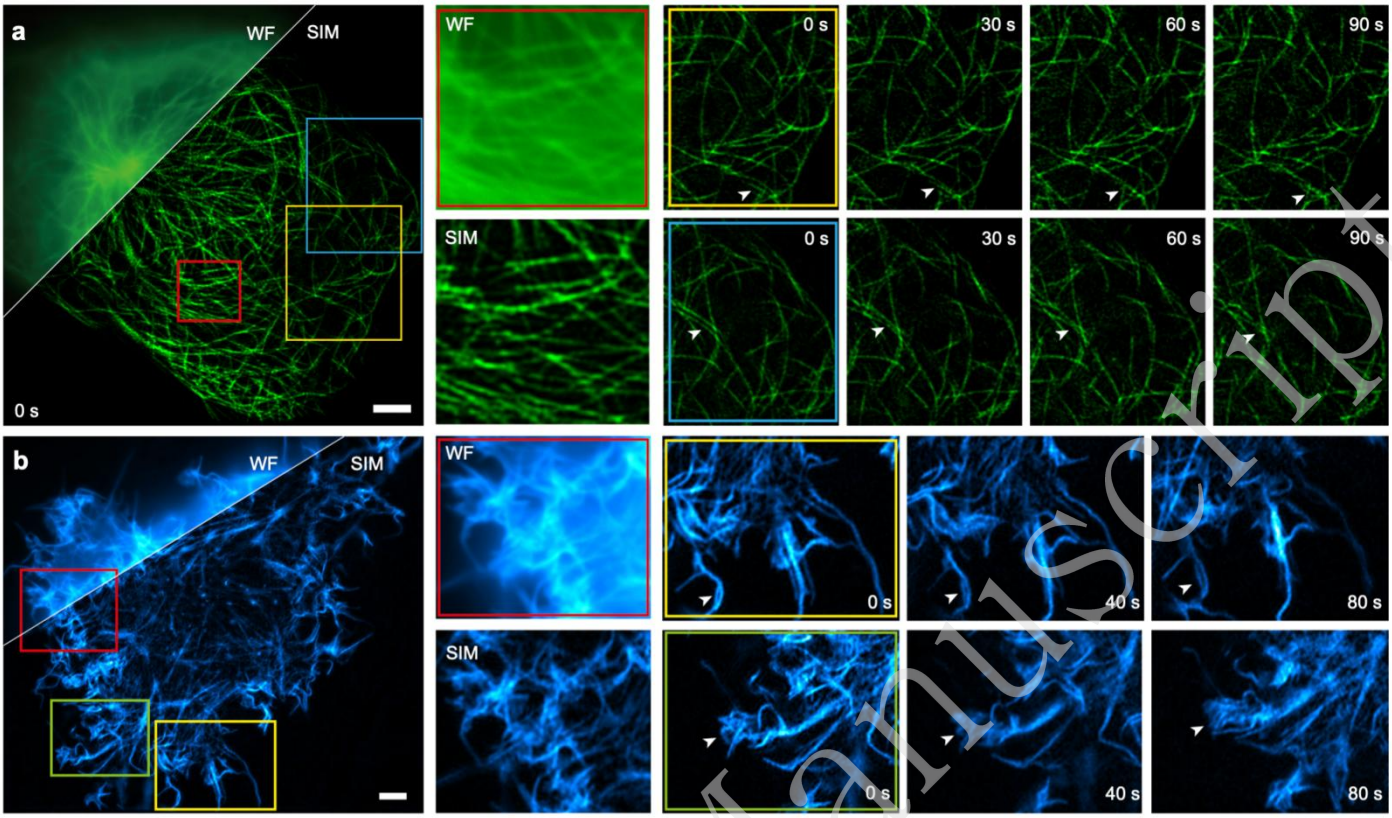

Fig. 5 | Time-lapse live-cell imaging with Sero-SIM. a, Microtubules in live U2OS cells. Resolution improvement comparison is presented in the red box. Time-lapse imaging of the white and the orange regions is shown from 0 to 90 s on the right. **b**, Actin filaments in live COS-7 cells. Resolution improvement comparison is presented in the red box. Time-lapse imaging of the orange region is shown from 0 s to 210 s on the right. Scale bars: 4 μm (**a, b**).

magnification and NA provide a larger FOV and greater depth of focus (DOF), which are advantageous for the high-resolution imaging of cell populations.

At lower magnification (20×/0.80 NA), Sero-SIM achieves an FOV of 393 μm × 393 μm, enabling large-area super-resolution fluorescence imaging of histological specimens. We imaged a transverse section of *Nerium oleander* leaf tissue and clearly resolved multiple layers of palisade mesophyll, spongy mesophyll, and epidermal cells (Fig. 4g).[47] Under wide-field fluorescence illumination, the cuticle and thickened cell walls exhibited strong autofluorescence, and together with the out-of-focus background, structural details appeared as continuous bright patches. In contrast, Sero-SIM super-resolution imaging with dark sectioning effectively suppressed background blur and distinctly resolved adjacent cell walls, even in thick leaf tissues.[40] Moreover, Sero-SIM revealed ladder-like periodic patterns along the trichomes within the stomatal crypts, corresponding to the stepwise thickening of cell walls in these hair-like protrusions (Fig. 4h). These results, obtained under low-magnification objectives, highlighted the capability of Sero-SIM to deliver large-field, high-contrast, and high-resolution imaging of plant tissues.

At 60× magnification (1.40 NA), corresponding to an FOV of 166 μm × 166 μm, we imaged mitochondria labelled with MitoTracker Red™ CMXRos in bovine pulmonary artery endothelial (BPAE) cells, visualising the perinuclear mitochondrial network (Fig. 4i, j). In wide-field fluorescence imaging, mitochondrial structures appeared as blurred, continuous filaments owing to their limited resolution and out-of-focus background. In contrast, Sero-SIM clearly resolved the sub-branches and ring-like segments within the mitochondrial network, confirming its suitability for large-FOV super-resolution organelle imaging.

In a breast cancer tissue section, bright-field, wide-field fluorescence, and SIM imaging were performed using a 10×/ 0.45 NA objective, providing an FOV of over 1 mm^2 (Fig. 4k). Bright-field imaging revealed the overall tissue organisation (Fig. 4l). Because lipid components exhibit weak autofluorescence in fluorescence imaging, the absence of strong lipid-derived signals facilitated the visualisation of other tissue structures. Sero-SIM distinctly delineated the boundaries of the nuclei and cytoplasmic vacuoles, which appeared as bright-ring and hollow-centred structures (Fig.

Accepted Manuscript

ACCEPTED ARTICLE PREVIEW

4m, n). This morphology correlates with enlarged nuclei and increased nuclear-to-cytoplasmic ratio characteristic of breast cancer cells.[48,49] The fluorescence signal within the nuclear region was relatively weak, likely owing to the low abundance of endogenous fluorophores and the strong absorption and scattering of both excitation and emission light by densely packed chromatin.

Collectively, these experiments demonstrated that Sero-SIM bridges multiple biological scales, enabling researchers to explore tissue-level pathology with cellular-scale FOV and subcellular-scale resolution. This multiscale imaging capability provides Sero-SIM with considerable potential for clear and diagnostically informative visualisation.

Time-lapse super-resolution imaging in live cells

The low phototoxicity and reduced photobleaching inherent to SIM make it an effective technique for dynamic live-cell imaging. Sero-SIM can be used for time-lapse super-resolution imaging of live cells. We labelled tubulin in live U2OS cells with EMTB-mYongHong and acquired nine raw images every 30 s to continuously monitor the dynamic reorganisation of the microtubule cytoskeleton at subdiffraction resolution. As shown in Fig. 5a, individual microtubule filaments were clearly resolved and their dynamic behaviours, including extension, retraction, and network rearrangement, were readily visualised over tens of seconds. The formation and dissolution of local bundles, along with fluctuations in filament curvature and intersections, revealed the intrinsic dynamic instability of microtubules. We also labelled actin filaments in live COS-7 cells and recorded their movement over extended periods (Fig. 5b). Owing to the sample thickness, wide-field fluorescence imaging suffered from strong background noise. Sero-SIM substantially improved both the signal-to-background ratio and spatial resolution, revealing finer subcellular details. These live-cell experiments demonstrated the stability, robustness, and low phototoxicity of Sero-SIM during dynamic imaging.

Discussion

In contrast to mainstream SIM architectures that rely on digital diffraction devices such as SLMs or DMDs, Sero-SIM employs a nine-sector grating roulette driven by a piezoelectric rotation mount as its core optical component. This design enables the efficient modulation of both the illumination direction and phase at a hardware cost far lower than that of conventional digital approaches. The entire system requires only two active components, the camera and rotary stage, whose synchronisation can be managed through a simple MATLAB or Python programme, thereby significantly reducing the system-control complexity and operational barriers. Through a series of experiments, we demonstrated that the ultra-low-cost Sero-SIM achieves super-resolution imaging with an FOV exceeding 1650 pixels×1650 pixels and an approximately twofold resolution enhancement. It successfully resolves diverse biological structures across multiple spatial scales ranging from tissue sections to cytoskeletal networks. Delivering high resolution, large FOV, and outstanding cost efficiency (Supp. Table 4), Sero-SIM can be widely applied across biological research, medical diagnostics, and clinical pathology.

The key to reducing the system cost is to replace the digital diffractive modulators with a custom-designed grating roulette, which provides a higher diffraction efficiency and superior beam quality. In our approach, only rotational switching is used to modulate both the phase shift and angular orientation of the structured illumination patterns. Unlike pixelated digital devices such as SLMs or DMDs, which generate redundant two-dimensional diffraction orders, the binary-amplitude grating employed here efficiently produces diffraction exclusively in the intended direction. Future implementations could further enhance the diffraction efficiency by adopting phase or polarisation gratings. In addition, SLMs are not suitable for ultraviolet diffraction owing to the strong absorption of liquid crystals in the UV band, whereas DMDs have very limited performance in multicolour imaging owing to their blazed grating effect.[27,29] In contrast, for physical transmission gratings, although the diffraction angle changes with wavelength according to the grating equation, the grating itself remains effective over a broad spectral range and shows better scalability for UV illumination. Despite the non-achromatic grating roulette and pyramidal lens, in multi-colour imaging, the chromatic dispersion in the Sero-SIM system can be compensated by slightly adjusting the position of the pyramidal lens along the optical axis because the pyramidal lens changes the propagation direction of the beams without affecting their collimation, effectively dividing the excitation path into two independent segments (Fig. S2).

Although the introduction of a pyramidal lens in this system decouples the sector grating size from the FOV, thereby enabling large-FOV imaging, the imaging speed remains limited by the mechanical rotation rate of the roulette. Experiments show that it takes 3.3 s on average and nine raw frames with an exposure time of 30 ms (Supp. Table 2,

3). This constraint currently prevents the capture of sub-second biological dynamics in live-cell imaging. Excitingly, recent technological developments have led to faster and more precise rotation motors, which may improve the imaging speed of Sero-SIM by many times and address its greatest current limitation. Specifically, as detailed in Supp. Note 6, upgrading from our current piezoelectric actuator to state-of-the-art direct-drive or low-inertia frameless torque motors can reduce the theoretical 40° positioning time from 93 ms to the sub-10-ms regime. While we acknowledge the practical nuances of dynamic settling times, these metrics firmly establish the engineering feasibility of increasing the speed of the Sero-SIM by at least an order of magnitude, laying the foundation for near-video-rate acquisition.

Additionally, as a system inherently based on the 2D-SIM principle, the thick-sample imaging capability of Sero-SIM remains limited. Dark sectioning is applied for background suppression, allowing imaging of moderately thick biological tissues. For deeper imaging beyond 20 μm, integrating optical sectioning techniques such as light-sheet illumination or adaptive optics can further improve axial imaging depth.[50,51] In large-FOV imaging, non-uniform sample thickness poses an additional challenge in maintaining all regions in focus simultaneously. Sequential axial scanning of the focal plane can effectively reconstruct a clear three-dimensional view of a specimen.

Sero-SIM introduces a novel and distinctive approach for SIM implementation by efficiently integrating pattern rotation and phase shifting within a diffractive element at an exceptionally low cost. The design of the grating roulettes is highly flexible and amenable to customisation. For instance, by retaining the zeroth-order diffraction beam and increasing the number of sectors, Sero-SIM can be extended from 2D-SIM to 3D-SIM, thereby enabling axial resolution enhancement. Beyond SIM, the concept of a grating roulette also provides a new paradigm for optical diffraction modulation, potentially facilitating flexible mode switching across various microscopy modalities and further advancing the accessibility of high-performance imaging technologies.

Acknowledgements

This work was supported by the Major Basic Research Project of the Natural Science Foundation of Shandong Province (ZR2024ZD27), the Beijing Science and Technology Program (Z251100006925026), the National Natural Science Foundation of China (62025501, 62335008, 92150301, 62411540238, and 624B2009), and the National Key R&D Program of China (2022YFC3401100).

Author contributions

P.X. and M.L. supervised the study. H.W., R.C., and P.X. initiated and conceived the study. H.W. and R.C. designed the optical layout, built the Sero-SIM system, performed the experiments, analysed the data, and prepared the figures under the guidance of P.X. and M.L. R.C. and W.W. developed the algorithm and performed the reconstruction. W.R. helped customise the grating roulette. J.R. investigated the costs of various SIM implementations. S.G., H.W., Y.F., L.L., and M. T. prepared live U2OS cell samples. H.W., R.C., M.L., and P.X. wrote the manuscript with input from all the authors. All authors participated in the work involved in this study.

Data availability

Software and typical data of Sero-SIM are uploaded to GitHub: https://github.com/Cao-ruijie/SeroSIM.

Conflict of interests

Dr. Peng Xi holds the position of Chief Technology Officer (CTO) at Airy Technologies. He declares that there are no additional financial or personal interests that could be perceived as conflicts of interest in relation to the research presented in this paper. The other authors declare no competing interests.

References

1. Heintzmann, R. & Huser, T. Super-resolution structured illumination microscopy. *Chemical Reviews* **117**, 13890-13908 (2017).
2. Sigal, Y. M., Zhou, R. B. & Zhuang, X. W. Visualizing and discovering cellular structures with super-resolution microscopy. *Science* **361**, 880-887 (2018).

Accepted Manuscript

ACCEPTED ARTICLE PREVIEW

3. Wu, Y. C. & Shroff, H. Faster, sharper, and deeper: structured illumination microscopy for biological imaging. *Nature Methods* **15**, 1011-1019 (2018).
4. Schermelleh, L. et al. Super-resolution microscopy demystified. *Nature Cell Biology* **21**, 72-84 (2019).
5. Wang, H. et al. High-spatiotemporal-resolution structured illumination microscopy: principles, instrumentation, and applications. *Photonics Insights* **4**, R01 (2025).
6. Gustafsson, M. G. L. Surpassing the lateral resolution limit by a factor of two using structured illumination microscopy. *Journal of Microscopy* **198**, 82-87 (2000).
7. Gustafsson, M. G. L. Nonlinear structured-illumination microscopy: wide-field fluorescence imaging with theoretically unlimited resolution. *Proceedings of the National Academy of Sciences of the United States of America* **102**, 13081-13086 (2005).
8. Gustafsson, M. G. L. et al. Three-dimensional resolution doubling in wide-field fluorescence microscopy by structured illumination. *Biophysical Journal* **94**, 4957-4970 (2008).
9. N-SIM E Super-Resolution Microscope. (2016). at https://www.microscope.healthcare.nikon.com/zh_CN/products/super-resolution-microscopes/n-sim-e
10. Chen, X. et al. Superresolution structured illumination microscopy reconstruction algorithms: a review. *Light: Science & Applications* **12**, 172 (2023).
11. Fiolka, R., Beck, M. & Stemmer, A. Structured illumination in total internal reflection fluorescence microscopy using a spatial light modulator. *Optics Letters* **33**, 1629-1631 (2008).
12. Chang, B. J. et al. Isotropic image in structured illumination microscopy patterned with a spatial light modulator. *Optics Express* **17**, 14710-14721 (2009).
13. Kner, P. et al. Super-resolution video microscopy of live cells by structured illumination. *Nature Methods* **6**, 339-342 (2009).
14. Shao, L. et al. Super-resolution 3D microscopy of live whole cells using structured illumination. *Nature Methods* **8**, 1044-1046 (2011).
15. Fiolka, R. et al. Time-lapse two-color 3D imaging of live cells with doubled resolution using structured illumination. *Proceedings of the National Academy of Sciences of the United States of America* **109**, 5311-5315 (2012).
16. Förster, R. et al. Simple structured illumination microscope setup with high acquisition speed by using a spatial light modulator. *Optics Express* **22**, 20663-20677 (2014).
17. Lu-Walther, H. W. et al. fastSIM: a practical implementation of fast structured illumination microscopy. *Methods and Applications in Fluorescence* **3**, 014001 (2015).
18. Song, L. Y. et al. Fast structured illumination microscopy using rolling shutter cameras. *Measurement Science and Technology* **27**, 055401 (2016).
19. Huang, X. S. et al. Fast, long-term, super-resolution imaging with Hessian structured illumination microscopy. *Nature Biotechnology* **36**, 451-459 (2018).
20. Li, X. S. et al. Three-dimensional structured illumination microscopy with enhanced axial resolution. *Nature Biotechnology* **41**, 1307-1319 (2023).
21. Xu, X. Z. et al. Ultra-high spatio-temporal resolution imaging with parallel acquisition-readout structured illumination microscopy (PAR-SIM). *Light: Science & Applications* **13**, 125 (2024).
22. Fu, Y. Z. et al. Triangle-beam interference structured illumination microscopy. *Nature Photonics* **19**, 1122-1131 (2025).
23. York, A. G. et al. Resolution doubling in live, multicellular organisms via multifocal structured illumination microscopy. *Nature Methods* **9**, 749-754 (2012).
24. Dan, D. et al. DMD-based LED-illumination super-resolution and optical sectioning microscopy. *Scientific Reports* **3**, 1116 (2013).
25. Li, M. Q. et al. Structured illumination microscopy using digital micro-mirror device and coherent light source. *Applied Physics Letters* **116**, 233702 (2020).
26. Lachetta, M. et al. Dual color DMD-SIM by temperature-controlled laser wavelength matching. *Optics Express* **29**, 39696-39708 (2021).
27. Gong, D. Z. et al. Easily scalable multi-color DMD-based structured illumination microscopy. *Optics Letters* **49**, 77-80 (2024).
28. Wang, H. et al. 3D gradient printing based on digital light processing. *Journal of Materials Chemistry B* **11**, 8883-8896 (2023).
29. Li, Y. N. et al. High-speed autopolarization synchronization modulation three-dimensional structured illumination microscopy. *Advanced Photonics Nexus* **3**, 016001 (2023).
30. Wen, G. et al. Pyramidal lens enables mesoscale structured illumination by surpassing the spatial bandwidth limit of spatial light modulators. *Optica* **12**, 1180-1191 (2025).
31. Chen, X. et al. Diffraction of digital micromirror device gratings and its effect on properties of tunable fiber lasers. *Applied Optics* **51**, 7214-7220 (2012).
32. Lingel, C., Haist, T. & Osten, W. Optimizing the diffraction efficiency of SLM-based holography with respect to the fringing field effect. *Applied Optics* **52**, 6877-6883 (2013).
33. Popoff, S. M. et al. A practical guide to digital micro-mirror devices (DMDS) for wavefront shaping. *Journal of Physics: Photonics* **6**, 043001 (2024).

Accepted Manuscript

ACCEPTED ARTICLE PREVIEW

34. Schneider, C. A., Rasband, W. S. & Eliceiri, K. W. NIH Image to ImageJ: 25 years of image analysis. *Nature Methods* **9**, 671-675 (2012).
35. Müller, M. et al. Open-source image reconstruction of super-resolution structured illumination microscopy data in ImageJ. *Nature Communications* **7**, 10980 (2016).
36. Wen, G. et al. High-fidelity structured illumination microscopy by point-spread-function engineering. *Light: Science & Applications* **10**, 70 (2021).
37. Zhang, K., Li, L. L. & Liu, Q. Dark-field structured illumination microscopy for highly sensitive detection of 3D defects in optical materials. *Optics and Lasers in Engineering* **161**, 107340 (2023) doi: 10.1016/j.optlaseng.2022.107340.
38. Chen, X., Hou, Y. W. & Xi, P. Parameter estimation of the structured illumination pattern based on principal component analysis (PCA): PCA-SIM. *Light: Science & Applications* **12**, 41 (2023) doi: 10.1038/s41377-022-01043-9.
39. Liu, W. J. et al. Visualizing intraorganellar ultrastructures, dynamics, and interactions with open-access background-free Lock-in-SIM. *Nature Communications* **16**, 10765 (2025) doi: 10.1038/s41467-025-65805-w.
40. Cao, R. J. et al. Dark-based optical sectioning assists background removal in fluorescence microscopy. *Nature Methods* **22**, 1299-1310 (2025).
41. Backlund, M. P. et al. The role of molecular dipole orientation in single-molecule fluorescence microscopy and implications for super-resolution imaging. *ChemPhysChem* **15**, 587-599 (2014).
42. Camacho, R., Täuber, D. & Scheblykin, I. G. Fluorescence anisotropy reloaded—emerging polarization microscopy methods for assessing chromophores' organization and excitation energy transfer in single molecules, particles, films, and beyond. *Advanced Materials* **31**, 1805671 (2019).
43. Chandler, T. et al. Spatio-angular fluorescence microscopy I. Basic theory. *Journal of the Optical Society of America A* **36**, 1334-1345 (2019).
44. Zhanghao, K. et al. High-dimensional super-resolution imaging reveals heterogeneity and dynamics of subcellular lipid membranes. *Nature Communications* **11**, 5890 (2020).
45. Cao, R. J. et al. Open-3DSIM: an open-source three-dimensional structured illumination microscopy reconstruction platform. *Nature Methods* **20**, 1183-1186 (2023).
46. Heyting, C. Synaptonemal complexes: structure and function. *Current Opinion in Cell Biology* **8**, 389-396 (1996).
47. Evert, R. F. Esau's Plant Anatomy: Meristems, Cells, and Tissues of the Plant Body: Their Structure, Function, and Development. (Hoboken: John Wiley & Sons, Inc, 2006).
48. Weigelt, B., Geyer, F. C. & Reis-Filho, J. S. Histological types of breast cancer: how special are they?. *Molecular Oncology* **4**, 192-208 (2010).
49. Veta, M. et al. Breast cancer histopathology image analysis: a review. *IEEE Transactions on Biomedical Engineering* **61**, 1400-1411 (2014).
50. Kang, S. et al. High-resolution adaptive optical imaging within thick scattering media using closed-loop accumulation of single scattering. *Nature Communications* **8**, 2157 (2017).
51. Temma, K. et al. Selective-plane-activation structured illumination microscopy. *Nature Methods* **21**, 889-896 (2024).

Accepted Manuscript

ACCEPTED ARTICLE PREVIEW

Methods

Sero-SIM microscope

The optomechanical design of the Sero-SIM microscope is shown in Fig. 1. The number of mirrors shown in Fig. 1a is for reference only. In an actual optical setup, some mirrors may be removed to keep the system simple and compact. The system consists of the following components:

Laser sources and beam expander. In Sero-SIM, laser sources with wavelengths of 473 and 561 nm (MBL-III-473-100 mW, CNI; MGL-FN-561-200mW, CNI) are employed for fluorescence excitation. The laser beams were combined into a common optical path by using a dichroic mirror (DM1, DMR-505LP, LBTEK). A pair of achromatic lenses (BE1, f=30 mm, MAD405-A, LBTEK; BE2, f=100 mm, MAD408-A, LBTEK) expands the beam diameter by 3.3 times to illuminate the working sector of the grating roulette uniformly. To avoid the diffraction of other grating sectors, a diaphragm (DP12, LBTEK) is placed before the grating roulette.

Grating roulette and rotation mount. The grating constant of each sector is 62.5 μm, corresponding to a diffraction angle of 0.514° for a wavelength of 561 nm according to the grating equation. Line pairs of different directions and phases are first generated using Mathematica (Wolfram Research) and then exported to the DWG format, which can be edited using AutoCAD (Autodesk). A customised binary grating roulette is produced by Juzhike Optoelectronics. The grating roulette was installed on a rotation mount with a resonant piezoelectric motor (Thorlabs ELL14K). To ensure the position accuracy of the grating roulette, we use an x-y translation stage (GCM-122101M, Daheng Optics) for precise adjustment. The diffracted light beams are converged by an achromatic lens (L1, f=200 mm, MAD418-A, LBTEK) and then collimated by a concave lens (L2, f=-50 mm, MCX10510A, LBTEK). The collimated beams are refracted using a pyramidal lens.

Pyramidal lens and polarisation modulation. The pyramidal lens is a transparent pyramid-shaped refractive element featuring six inclined polished facets and a hexagonal polished platform. Inclined surfaces are used to refract the illumination beams in three directions, whereas the platform was designed to transmit the 0th-order beam. The apex angle refers to the angle between each inclined facet and the platform plane. A larger apex angle results in a stronger refraction of the incident light. A pyramidal lens is a customised optical component. In Sero-SIM, the pyramidal lens made of NBK-7 glass has an apex angle of 16.65°. The pyramidal lens is manufactured by Jiangnan Optics (China). For multi-colour imaging, the pyramidal lens is mounted on a dovetail rail (DR50-150, LBTEK). After passing through the pyramidal lens, the 0th beam is blocked with a customised spatial filter (mask), while the first-order beams pass through. The collimated first-order beams intersect before L3 (f=19 mm, MAD303-A, LBTEK). L3 and L4 (f=250 mm, OLD2468-T2M, JCOPTIX) function as a 4f system, expanding the beam diameters by 13.1 times. S-polarised light is required to improve the modulation depth of the structural illumination patterns. The light from the laser source is linearly polarised. When passing through a linear polariser (LP, FLP25-VIS-M, LBTEK), the polarisation linearity improves without significant energy wastage. The polarised light then passes through different sectors of an achromatic six-segment waveplate (AHWP25-VIS-A-6P-M, LBTEK), which rotates the polarisation direction of the incident beams to s-polarised states. The mirrors after (M7-9) should keep the main optical axis of the system strictly parallel to the optical platform to avoid severe polarisation degradation induced by reflection.

Fluorescence excitation and emission detection. Lens L5 (f=200 mm, OLD2466-T2M, JCOPTIX) focuses the first-order diffracted beams on the back focal pupil (BFP) of the objectives (CFI Plan Apochromat Lambda D 100X Oil, NA 1.45, Nikon; CFI Plan Apochromat Lambda 60X Oil, NA 1.40, Nikon; CFI Plan Apochromat Lambda D 40X, NA 0.95, Nikon; CFI Plan Apochromat Lambda D 20X, NA 0.8, Nikon; CFI Plan Apochromat Lambda D 10X, NA 0.45, Nikon). A polarisation-maintaining dichroic mirror DM2 (ZT405/473–488/561/640 rpc-Phase R-UF3, Chroma) prevents degradation of the polarisation states of the incident light beams. A tube lens (TL, TTL200-A, Thorlabs) focuses the fluorescence emission onto a scientific complementary metal–oxide–semiconductor (sCMOS) camera (ORCA-Flash4.0 V2, Hamamatsu) after passing through an emission filter (ZET405/473/561/640m, Chroma). With a pyramidal lens, Sero-SIM achieves an FOV of approximately 2048 pixels× 2048 pixels, covering the entire area of the

ACCEPTED ARTICLE PREVIEW

sCMOS sensor. However, to obtain uniform illumination with Gaussian beams, the effective FOV for Sero-SIM is approximately 1650 pixels× 1650 pixels, which is shown in Fig. 2.

Sero-SIM system calibration

The basic key points of Sero-SIM alignment are similar to those of mainstream SIM implementations. The absence of digital diffraction devices such as SLMs and DMDs spares some corresponding alignment steps, whereas the presence of a grating roulette and pyramidal lens introduces some new calibration procedures. For Sero-SIM, the grating roulette is recommended to be installed on a simple translation stage for position adjustment along or perpendicular to the main optical axis to ensure phase-shift accuracy.

One of the key procedures for Sero-SIM calibration is to precisely adjust the distance between L3 and the pyramidal lens. Without the spatial filter, the 0th- and ±1st-order beams will be useful in calibration. First, when Sero-SIM is used for multicolour imaging, the pyramidal lens should be installed on a dovetail rail or a translation stage that is strictly parallel to the main optical axis, ensuring that the translation of the pyramidal lens causes no change in the 0th diffracted beam. Secondly, temporarily replace the pyramidal lens with a convex lens (L') which converges the collimated beams to its focal point. An interferometer was positioned immediately after lens L3 to examine the light collimation. By translating lens L' along the dovetail rail, the collimated light can be detected in the interferometer. Using an observation screen, we can mark the precise position of L3's front focal point, noted as F1. After replacing L' with the pyramidal lens again, the pyramidal lens should be moved to an appropriate position where the ±1st-order beams of a certain working wavelength intersect precisely on F1. A detailed illustration of chromatic aberration compensation is provided in Fig. S2d.

The other key procedure is phase-shift correction, which should be performed after establishment and careful alignment of the complete Sero-SIM system. Samples with strong autofluorescence, such as onion root tip cells, where stripe patterns are sufficiently clear to be observed, are recommended for phase-shift correction. After nine raw images are obtained, stripe patterns will be visible on the raw images. Because of the limited absolute positioning accuracy, the phase shift in the three directions may not be ideal. By introducing a subtle rotation angle disturbance from [120°, 160°, 200°] to [120°, 160.1°, 200.05°], for instance, the phase-shift uncertainty can be well compensated because the rotation mount offers sufficient bidirectional positioning accuracy. This was repeatedly confirmed in our experiments. The concrete values of the angular disturbance can be determined after a few trials. A subtle translation of the grating roulette will be useful in scenarios where the stripes on the grating are tangential to its rotation direction (sectors IV, V, and VI in Fig. 1b). With Sero-SIM reconstruction algorithms, very accurate and ideal phase shifts as in conventional SIM techniques should be pursued, and avoiding extreme scenarios that might have very few phase shifts is sufficient, as discussed in Fig. S4 and Supp. Note 4. Approximately 10 min is required to correct the phase-shift uncertainty by angle disturbance, and the recommended correction frequency is once a week.

Hardware control and timing synchronization

Sero-SIM has only two active components: the rotation mount and sCMOS camera. A simple MATLAB programme is used for their control and synchronisation. The Image Acquisition Toolbox (available in MATLAB add-ons) and DCAM-API (Hamamatsu SDK, available on the Hamamatsu website) should be installed in advance. As the main limitation of the imaging speed lies in the mechanical rotation of the grating roulette, a computer can work as the master of the two active components without considering extra time consumption. We also provided a system-control programme written in Python for better hardware support. Sero-SIM synchronisation is illustrated in Fig. S3.

SIM reconstruction

The reconstruction of Sero-SIM partially follows traditional SIM algorithms. First, dark sectioning is used to process the raw images and remove the out-of-focus background. The raw images are then summed to form a simulated WF image with notched frequency peaks. After the frequency and angle of the illumination patterns are estimated, simulated illumination is used to multiply the simulated widefield images with phase changes. The correlation between simulated raw images and actual raw images is calculated to determine the correct phase of the illumination pattern. Subsequently, phase separation and frequency shift are conducted using the correct phase. We designed a two-

ACCEPTED ARTICLE PREVIEW

step filter with a notch filter to optimise the results. A notch filter is used to notch the frequency peak caused by the zero-frequency component and error between the calculated and actual phases. The two-step filter can further reduce the artefacts and maintain weak information. Finally, an inverse Fourier transform is performed to obtain the final super-resolution images. Additionally, note that in large-FOV scenarios, we split the images into four blocks for better reconstruction.[49,50] This significantly reduces the parameter error under uniform illumination. All reconstructions were performed using MATLAB 2021b (MathWorks).

Sample preparation, cell culture, and transfection

Fluorescent beads. Diluted fluorescent microsphere samples were prepared for system characterisation. High-precision glass coverslips were coated with poly-L-lysine solution [poly-L-lysine: ddH_2O: phosphate-buffered saline (PBS) = 3:1:1] (poly-L-lysine: Aladdin, P303253) at room temperature for no less than 30 min, enabling the positive ions in poly-L-lysine to bind effectively to the negative surfaces of the fluorescent microspheres. After coating, the coverslips were rinsed twice with deionised water and dried. Carboxylate-modified FluoSpheres™ microspheres (F10720, Thermo Fisher Scientific) were diluted in PBS to an appropriate concentration (typically 1:10,000 or 1:100,000 dilution), achieving a sparse monolayer distribution. A small droplet of the diluted suspension was placed at the centre of the coated coverslip and incubated for 1 min before removing excess liquid. The sample was then rinsed three times with ultrapure water to remove the unbound microspheres. Finally, an anti-fade mounting medium was added before sealing the coverslip. The fluorescent beads were used for imaging after overnight storage.

Cell culture and transfection. U2OS (CRL-3455, ATCC) and COS-7 (CRL-1651, ATCC) cell lines were maintained in Dulbecco's modified Eagle medium (DMEM, 11966025, Gibco) supplemented with 10% heat-inactivated foetal bovine serum (FBS, A5670701, Gibco), 50 U mL^{-1} penicillin, and 50 μg mL^{-1} streptomycin (15140148, Gibco). Cells were seeded onto a μ-Slide eight-well chamber (80827, ibidi) pre-coated with 5 μg mL^{-1} fibronectin (HX-FN-1S, Standard Imaging) and cultured at 37 °C in a humidified incubator with 5% CO_2 until reaching 70%–85% confluency. All plasmids used in this study were extracted using an endotoxin-free plasmid extraction kit (CW2105S, TIANGEN). Cells were subcultured for two to three generations to ensure optimal recovery and growth conditions. Prior to transfection, the cell culture medium was replaced with fresh Opti-MEM (31985062, Gibco). Transfection was performed using Lipofectamine 3000 (L3000001, Thermo Fisher Scientific) according to the manufacturer's instructions. After 8 h of incubation in the transfection mixture, the cells were washed once with PBS and incubated in fresh full culture medium at 37 °C in an incubator with 5% CO_2 and 95% humidity for approximately 24 h.

Fixed samples. For subcellular imaging, fixed samples of actin filaments, microtubules, nuclear pore complexes, and synaptonemal complexes were prepared. The labelling procedures followed the protocols reported previously.[22,51] For cell imaging, we bought a FluoCells™ prepared slide of BPAE cells (with MitoTracker Red™ CMXRos, Alexa Fluor™ 488 phalloidin, and DAPI, 2329865, Thermo Fisher Scientific). For tissue imaging, we obtained a transverse section of *Nerium oleander* leaf and a section of breast cancer tissue (Vic Science and Education).

References

52. Hoffman, D. P. & Betzig, E. Tiled reconstruction improves structured illumination microscopy. *BioRxiv*, 2020. 2001. 2006. 895318 (2020).
53. Qian, J. et al. Principal component analysis for three-dimensional structured illumination microscopy (PCA-3DSIM). *Light: Science & Applications* **14**, 299 (2025).
54. Zhanghao, K. et al. Super-resolution imaging of fluorescent dipoles via polarized structured illumination microscopy. *Nature Communications* **10**, 4694 (2019).

Additional information

Supplementary information.

Correspondence and requests for materials should be addressed to Ruijie Cao, Meiqi Li, or Peng Xi.

Accepted Manuscript